# Assessment of Lesion Detectability in Dynamic Whole-Body PET Imaging Using Compartmental and Patlak Parametric Mapping

*Neda Zaker, MS,\*† Fotis Kotasidis, PhD,\* Valentina Garibotto, MD,\* and Habib Zaidi, PhD\*‡§//*

**Purpose:** Hybrid dynamic imaging allows not only the estimation of whole-body (WB) macroparametric maps but also the estimation of microparameters in the initial bed position targeting the blood pool region containing the pathology owing to the limited axial field of view of PET scanners. In this work, we assessed the capability of multipass WB $^{18}$F-FDG PET parametric imaging in terms of lesion detectability through qualitative and quantitative evaluation of simulation and clinical studies.

**Methods:** Simulation studies were conducted by generating data incorporating 3 liver and 3 lung lesions produced by 3 noise levels and 20 noise realizations for each noise level to estimate bias and lesion detection features. The total scan time for the clinical studies of 8 patients addressed for lung and liver lesions staging, including dynamic and static WB imaging, lasted 80 minutes. An in-house–developed MATLAB code was utilized to derive the microparametric and macroparametric maps. We compared lesion detectability and different image-derived PET metrics including the SUVs, Patlak-derived influx rate constant ($K_i$) and distribution volume ($V$) and $K_1$, $k_2$, $k_3$, blood volume (bv) microparameters, and $K_i$ estimated using the generalized linear least square approach.

**Results:** In total, 104 lesions were detected, among which 47 were located in the targeted blood pool bed position where all quantitative parameters were calculated, thus enabling comparative analysis across all parameters. The evaluation encompassed visual interpretation performed by an expert nuclear medicine specialist and quantitative analysis. High correlation coefficients were observed between $SUV_{max}$ and $K_{imax}$ derived from the generalized linear least square approach, as well as $K_i$ generated by Patlak graphical analysis. Moreover, 3 contrast-enhanced CT-proven malignant lesions located in the liver and a biopsy-proven malignant liver lesion not visible on static SUV images and Patlak maps were clearly pinpointed on $K_1$ and $k_2$ maps.

**Conclusions:** Our results demonstrate that full compartmental modeling for the region containing the pathology has the potential of providing complementary information and, in some cases, more accurate diagnosis than conventional static SUV imaging, favorably comparing to Patlak graphical analysis.

**Key Words:** compartmental modeling, lesion detectability, oncology, Patlak graphical analysis, PET

(*Clin Nucl Med* 2020;45: e221–e231)

PET is a powerful imaging modality for the noninvasive assessment of physiological and biological processes in vivo at the molecular level. Following intravenous injection of a positron-emitting probe into a patient in tracer quantities, PET can detect its biodistribution inside the body to assess a number of biological and physiological processes, such as glucose metabolism, perfusion, and proliferation.[1] Static PET data acquisition providing the spatial distribution of activity concentration within a fixed period of time represents the current standard for qualitative assessment through visual inspection and interpretation of the reconstructed images in clinical setting. However, additional underlying biological and physiological processes in tissues can be noninvasively characterized and quantitatively evaluated taking into account the temporal information using dynamic PET imaging, which proved useful in a variety of medical and clinical research scenarios,[2–4] such as diagnosis and therapy monitoring.[5,6]

In clinical setting, nuclear medicine physicians commonly review PET images to discriminate malignant disease from normal uptake patterns, inflammation areas, or artifacts based on their experience and medical knowledge.[7] Image analysis is often a qualitative process with physicians providing their assessment of visible features, sometimes evidenced by semiquantitative analysis particularly using SUV.[8] In some cases, the measurement of activity concentration alone at fixed times of nonspecific tracers, such as FDG, does not allow distinguishing between malignant and benign lesions.[7–14]

A more thorough assessment of physiological parameters of interest can be obtained through tracer kinetic modeling using temporally continuous dynamic data, mainly limited to one bed position, thus confining its applicability to about 15- to 25-cm axial field of view (FOV) on commercially available PET scanners. However, the major contribution of whole-body (WB) PET imaging in clinical oncology lies in its ability to assess disease dissemination.[15] Lately, a new approach to clinical dynamic WB imaging has been proposed consisting of an initial blood pool (cardiac or aorta) scan, followed by a number of WB passes to estimate $K_i$ Patlak parametric images as well as full compartmental modeling by generalized linear least square (GLLS) parametric images.[16,17] Using this hybrid protocol, it is possible to simultaneously perform GLLS full compartmental modeling in the FOV covering the initial blood pool scan containing the pathology, as well as WB Patlak analysis. For kinetic parameter estimation, an arterial input function (IF) is required. In the imaging protocol that we used, a noninvasive image-derived IF was utilized. Depending on the location of the pathology, the initial blood pool scan can be chosen in the heart region, ascending or descending aorta. Because full compartmental modeling requires both full-time course of activity distribution and image-derived IF and owing to the limited axial FOV of clinical PET scanners, full compartmental modeling can be performed only in the initial bed position. Initial results have demonstrated superior tumor-to-background contrast, and improved variance of $K_i$ images can be obtained from GLLS modeling as compared to standard Patlak analysis.[17] Moreover, by applying the hybrid protocol, parametric images are also made available to clinicians enabling them to evaluate disease more comprehensively using clinically feasible dynamic imaging protocol.

In this work, we used simulated and clinical studies to compare lesion detectability between SUV, Patlak, and GLLS ^{18}F-FDG WB PET images. Clinical studies were obtained from patients undergoing ^{18}F-FDG WB PET for oncologic staging, whereas the simulation studies were generated using the XCAT phantom. Our ultimate aim is to assess the benefits of hybrid WB dynamic time-of-flight PET imaging in terms of lesion detectability when using Patlak and GLLS-based metrics.

## MATERIALS AND METHODS

### Patient Population and Data Acquisition and Processing

In this study, data of 8 patients referred for oncologic staging of liver and lung lesions by WB ^{18}F-FDG PET/CT were used. The study protocol was approved by the local ethics committee, and all patients gave written informed consent to participate. After injecting a standard ^{18}F-FDG activity of 3.5 MBq/kg (3.71 ± 1.05 MBq/kg), PET/CT scans were performed on a Siemens Biograph mCT scanner. The whole duration of the scanning protocol is approximately 80 minutes, consisting of sequential dynamic and static acquisitions. The first step is a low-dose CT scan (120 kVp and 80 mAs) for attenuation correction followed by a 6-minute dynamic single-bed acquisition for extracting the IF in the blood pool region, then a dynamic WB (head-to-thigh) scan at ever increasing time intervals in continuous bed motion (CBM) mode (3 scans at 5 mm/s, 5 scans at 4.4 mm/s, and 5 scans at 4 mm/s), and finally the acquisition of static SUV WB CBM scan of approximately 20 minutes (depending on the patient's length/weight) starting ~60 minutes after injection. A contrast-enhanced CT scan was also acquired (6/8 patients) for diagnostic purposes. Three-dimensional (3D) iterative ordinary Poisson-ordered subset expectation maximization algorithm was used for image reconstruction with 2 iterations and 21 subsets, including time-of-flight and resolution modeling and postreconstruction Gaussian filtering using 2-mm full width at half maximum.[18]

### Simulation Studies Using the XCAT Phantom

The XCAT human torso phantom was used for modeling the time-dependent activity maps for specific tissues and tumors commonly encountered in WB oncology PET studies.[19] In this study, respiratory or cardiac motion was not considered. Six lesions of varying size were embedded in the lung (3) and liver (3). Two lung lesions have the same size but different microparameters, whereas the 3 liver lesions have the same microparameters but different sizes. The XCAT phantom consists of 67 regions including the tumors. For simulating dynamic WB CBM ^{18}F-FDG PET imaging, we implemented an in-house MATLAB code (MathWorks Inc) to assign realistic FDG kinetic microparameters and practicable blood volume values to the different regions (Table 1).[20] Time-activity curves are generated based on an IF, a temporal sampling protocol, and known tracer-specific pharmacokinetic parameters (constant rates), which control the bidirectional flux of the tracer between the blood and tissue compartments (for each organ structure in the anatomical phantom). The IF is derived from arterial sampling based on a parameterized model.[20] For the sampling protocol, 33 frames (20 cardiac frames and 13 passes) were used. To simulate the real protocol used for patient scanning, the 20 cardiac frame durations were similar to the clinical protocol (time frames of 8 × 5 seconds, 4 × 10 seconds, 4 × 25 seconds, and 4 × 45 seconds), whereas CBM data framing is fixed and dictated by the pass bed speed (3 × 44 seconds, 5 × 55 seconds, and 5 × 56 seconds). Figure 1 illustrates schematically the simulation process.

### Clinical Image Analysis

#### Visual Interpretation

SUV and parametric images of $K_i$-Patlak, V-Patlak, $K_i$-GLLS, $K_1$, $k_2$, $k_3$, and bv were spatially coregistered and evaluated visually by a nuclear medicine specialist. Images were rated as adequate/inadequate for visual interpretation and analyzed to identify the presence and anatomical localization of lesions visible either on the above image data sets or on the contrast-enhanced CT exclusively, namely, in the liver. The detected lesions were subsequently evaluated quantitatively.

On the basis of the electronic clinical records, including results of other imaging modalities and information derived from clinical follow-up, namely, biopsy results for 104 lesions, lesions were classified as malignant (biopsy-proven or proven by another imaging modality with high accuracy, such as contrast-enhanced CT for hepatocellular carcinoma [HCC]), benign (biopsy proven), probably malignant, and probably benign. To minimize the bias, we limited the number of analyzed lesions to 5 for organs or anatomical regions that had a higher number of lesions.

#### Quantitative Analysis of Simulation Studies

A 3D spherical region of interest (ROI) was manually drawn on each of the 6 lesions to extract the maximum and mean activity concentrations. Two distinct 3D spherical ROIs were also defined in the normal liver and normal lung regions defined as background. In addition to the maximum and mean values of each ROI, tumor-to-background ratio (TBR) and also contrast-to-noise ratio (CNR) were also calculated for all 20 noisy realizations of the 3 noise levels.

$$TBR = \frac{\text{Lesion ROI}_{max}}{\text{Background ROI}_{mean}} - 1 \qquad (1)$$

$$CNR = \frac{TBR}{\text{Background ROI}_{SD}} \qquad (2)$$

To quantify the bias and noise in the liver and lung ROIs of the derived parametric images, the normalized bias (NBias) and normalized SD (NSD) were calculated. Because the actual parameters (ground truth) are known for the simulated data, NBias for each region can be determined by first calculating $NBias_i$ for the *i*th voxel

**TABLE 1.** ^{18}F-FDG Kinetic Microparameters Used in Simulation Studies[25]

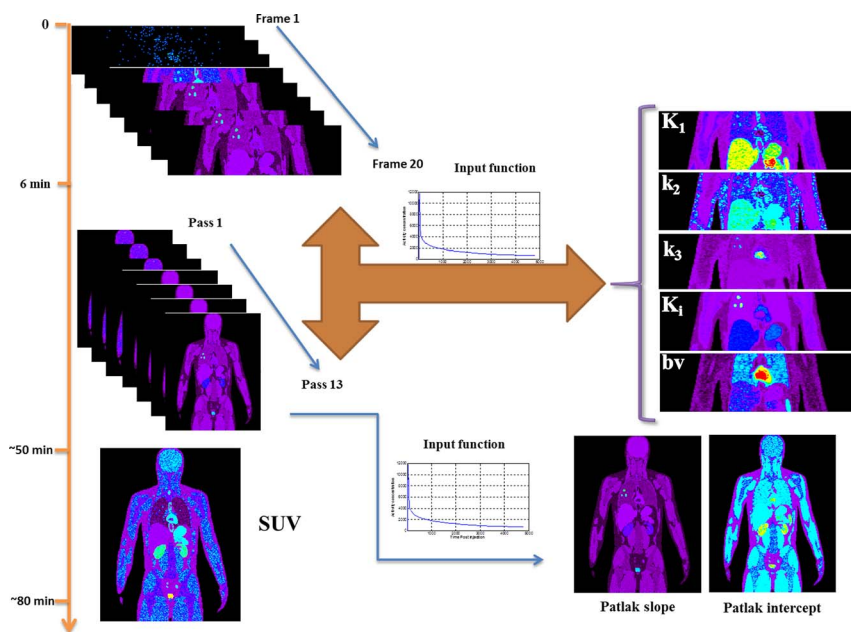| Regions | $K_1$, mL/min per mL | $k_2$, mL/min per mL | $k_3$, mL/min per mL | $k_4$, mL/min per mL | bv, mL/mL |
|---|---|---|---|---|---|
| Normal lung | 0.114 | 0.288 | 0.036 | 0 | 0.151 |
| Lung tumor 1 | 0.216 | 0.204 | 0.534 | 0 | 0.251 |
| Lung tumor 2 | 0.216 | 0.204 | 0.336 | 0 | 0.251 |
| Normal liver | 0.468 | 0.744 | 0.044 | 0 | 0.105 |
| Liver tumor | 1.056 | 1.032 | 0.318 | 0 | 0.205 |

**FIGURE 1.** Flowchart of the WB PET simulation protocol. The first dynamic acquisition is centered over the lower thorax/upper abdomen. The following 13 WB passes are acquired in CBM mode over the same axial length as the clinical SUV acquisition. By using the IF, acquired dynamic images, and the Patlak and GLLS analysis methods, macroparameters and microparameters are generated.

of an ROI over all 20 noise realizations and getting the average over all voxels of that ROI[2]:

$$\text{NBias} = \frac{1}{n} \sum_{i=1}^{n} \left( \frac{|\overline{f}_i - \mu_i|}{\mu_i} \right) \qquad (3)$$

where $\overline{f}_i = \left(\frac{1}{R}\right) \sum_{r=1}^{R} f_i^r$; $f_i^r$ corresponds to the $i$th voxel value from $r$th noise realization; $\mu_i$ denotes the reference true $i$th voxel value; $n$, the number of voxels in the ROI; and $R$, the number of noise realizations (20 in this work). Moreover, to calculate the NSD, first the $\text{NSD}_i$ of the $i$th voxel was calculated over all $R$ realizations followed by averaging over all $n$ voxels of the ROI.

$$\text{NSD} = \frac{1}{n} \sum_{i=1}^{n} \frac{\sqrt{\frac{1}{R-1} \sum_{r=1}^{R} \left( f_i^r - \overline{f}_i \right)^2}}{\overline{f}_i} \qquad (4)$$

The NSD index quantifies noise across multiple realizations of an ROI and in each voxel.

### Quantitative Analysis of Clinical Studies

A 3D spherical ROI was manually drawn on each lesion on all registered images of contrast-enhanced CT (whenever the contrast-enhanced CT was not available [2 of 8 patients], nonenhanced CT images have been used) and subsequently copied on SUV, Patlak slope, Patlak intercept, $K_i$-GLLS, $K_1$, $k_2$, $k_3$, and bv images. Background ROIs were also defined in nearby healthy surrounding tissues. The maximum and average values in the corresponding ROIs were calculated. In addition, the TBR and CNR scores were also calculated. Eventually, all identified lesions were grouped per organ regardless of the lesion type (primary tumor, metastasis, etc).

### Statistical Analysis

Spearman rank correlation coefficient ($\rho$) was used to assess the correlation between $\text{SUV}_{\text{max}}$ and other microparameters and

**TABLE 2.** Clinical Characteristics of the Patient Population and Anatomical Locations of the Detected Lesions

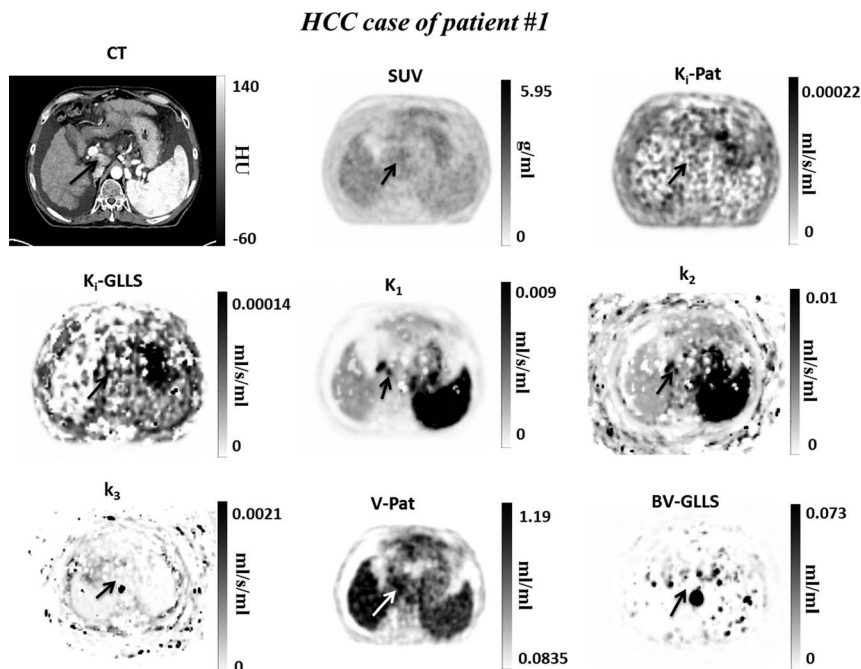| Patient No. | Age, y | Sex | Malignancy | Detected Lesions |
|---|---|---|---|---|
| 1 | 65 | Male | Hepatocellular carcinoma | Liver (3), parotid (1) |
| 2 | 74 | Male | Intrahepatic cholangiocarcinoma | Liver (5), abdominal lymph nodes (16), bone (1), Peritoneum (1), brain (1) |
| 3 | 45 | Female | Hepatic cholangiocarcinoma | Abdominal lymph nodes (9), lung (1), colon (2), liver (6), bone (4) |
| 4 | 45 | Female | Gastric adenocarcinoma | Stomach (2), bone (2), spleen (1), abdominal lymph node (2), brain (1) |
| 5 | 59 | Female | Lung neuroendocrine carcinoma | Mediastinal lymph nodes (4), adrenal gland (3), bone (1), lung (1) |
| 6 | 62 | Female | Lung adenocarcinoma | Lung (1), thyroid (1), rectum (1), colon (1) |
| 7 | 76 | Female | Lung adenocarcinoma | Mediastinal lymph node (2), lung (1), pleural nodule (2), bone (2) |
| 8 | 60 | Male | Hodgkin lymphoma | Lymph nodes (21), lung (1), subcutaneous nodule (1), intramuscular implant (1), bone (1) |

### HCC case of patient #1



**FIGURE 2.** Hepatocellular carcinoma case (patient 1), nonhypermetabolic on SUV and $K_i$-Patlak images and detected on $K_1$ and $k_2$ images. Top panel (from left to right): contrast-enhanced CT image, SUV PET image, and Patlak-derived influx rate constant ($K_i$-Pat). Middle panel (from left to right): GLLS-derived influx rate constant ($K_i$-GLLS) and rate constants ($K_1$ and $k_2$). Bottom panel (from left to right): rate constant ($k_3$), Patlak-derived distribution volume (V-Pat), and GLLS-derived blood volume (BV-GLLS).

macroparameters and between $K_{imax\text{-}Patlak}$ and $V_{max\text{-}Patlak}$ with other microparameters ($K_i$, $K_1$, $k_2$, $k_3$, bv). The correlation coefficient was calculated for all lesions and background ROIs. For this test, $P < 0.01$ was considered significant. Spearman correlation coefficient was also calculated for the six simulated lung and liver lesions considering the 3 noise levels and 20 noise realizations.

Therefore, we considered 3 (number of lesions per organ) × 3 (number of noise levels) × 20 (number of noise realizations) = 180 samples for both lung and liver separately for calculation of the correlation coefficients. The nonparametric Friedman test was performed on 18 malignant lesions located in the initial bed position for TBR and CNR scores to test for differences between 5 image
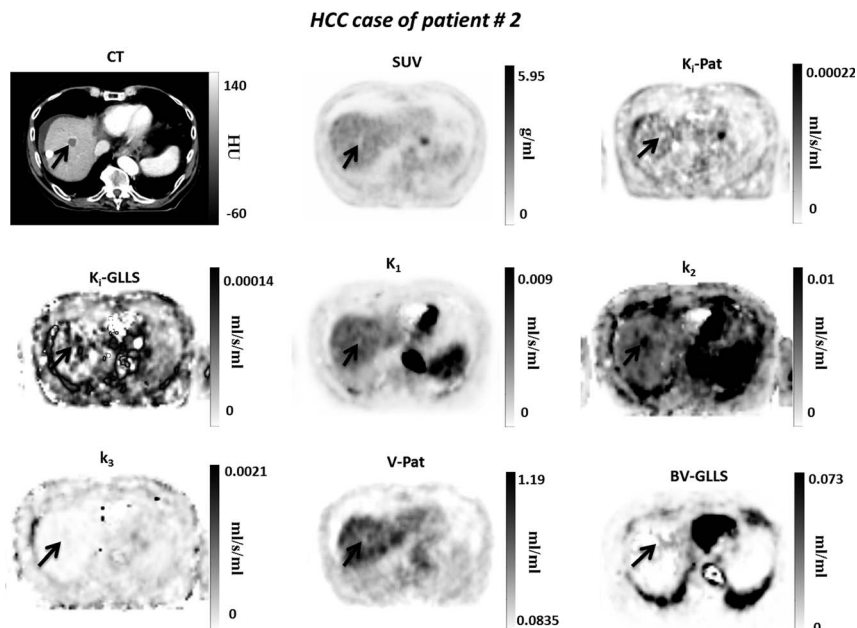
### HCC case of patient # 2



**FIGURE 3.** Case of an HCC (patient 2) detected only on $k_2$ image. The images shown are similar to Figure 2.

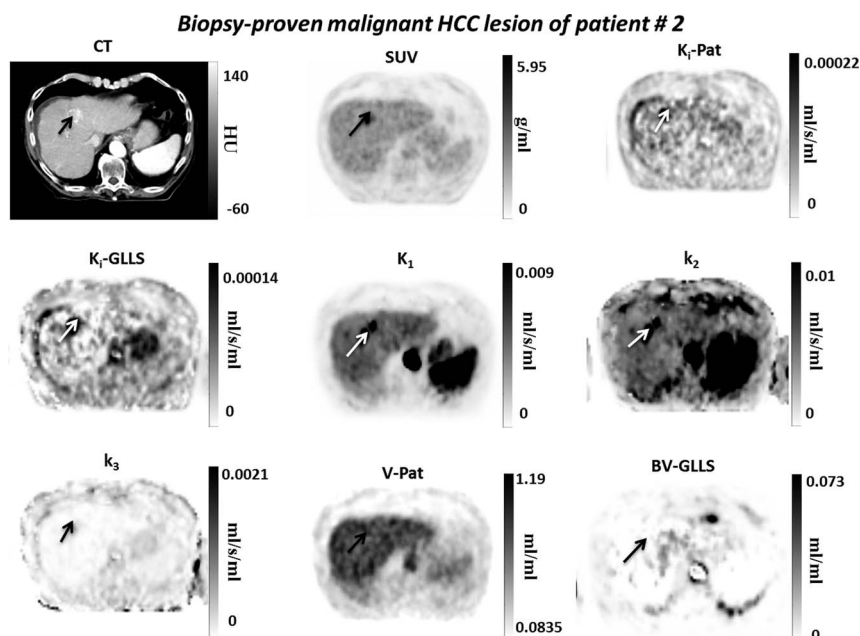**Biopsy-proven malignant HCC lesion of patient # 2**



**FIGURE 4.** Case of an HCC (patient 2), showing part of biopsy-proven malignant lesion (arrow) detected only on $K_1$ and $k_2$ images. It can be claimed that microparametric images complement information on lesion detection provided by the other modalities. The images shown are similar to Figure 2.

types ($K_i$-Patlak, $K_i$-GLLS, $K_1$, $k_2$, and $k_3$). $P = 0.05$ is considered significant for this test.

## RESULTS

Eight oncologic WB ^{18}F-FDG PET/CT studies (5 females and 3 males; mean age, $60.75 \pm 10.77$ years) were included in this study. Table 2 summarizes the clinical indications and the anatomical locations of the lesions assessed for each patient. The qualitative inspection of PET images revealed that all images were considered adequate for visual reading. The suppression of blood pool is obvious in $K_i$ images for organs that have nonnegligible fraction of blood pool compartment, such as the liver, spleen, and blood vessels (Figs. 2–5). This feature of $K_i$ images commonly results in higher contrast for lesions located close to these anatomical structures as reported in previous studies.[2,3,21–23] A total of 104 malignant lesions (n = 23), benign lesions (n = 2), probably malignant (n = 71), and probably benign (n = 8) were identified and analyzed.

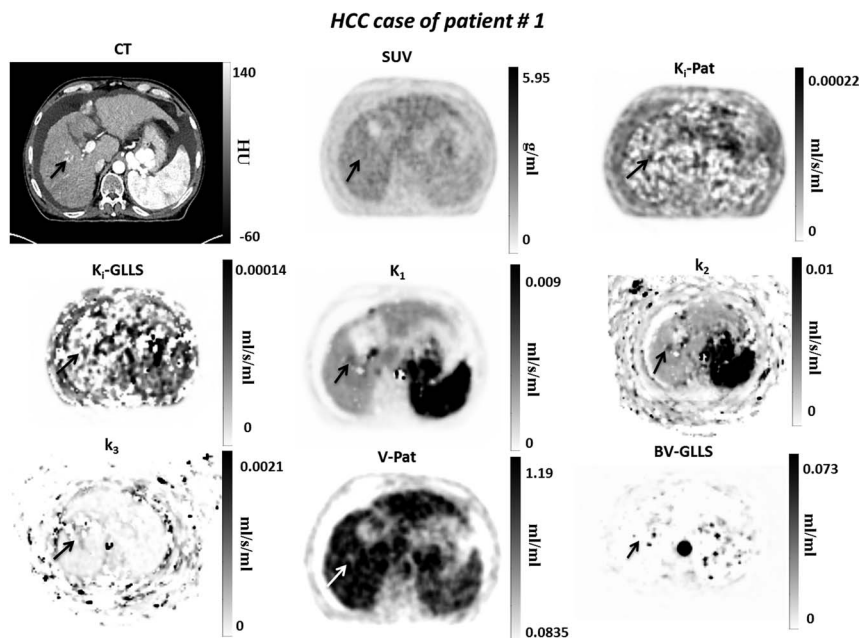**HCC case of patient # 1**



**FIGURE 5.** Case of an HCC (patient 1) detected on contrast-enhanced CT images, nonvisible in the SUV and $K_i$-Patlak, $k_3$, V-Patlak, and BV-GLLS images and visible on $K_i$-GLLS, $K_1$, and $k_2$ images. The images shown are similar to Figure 2.
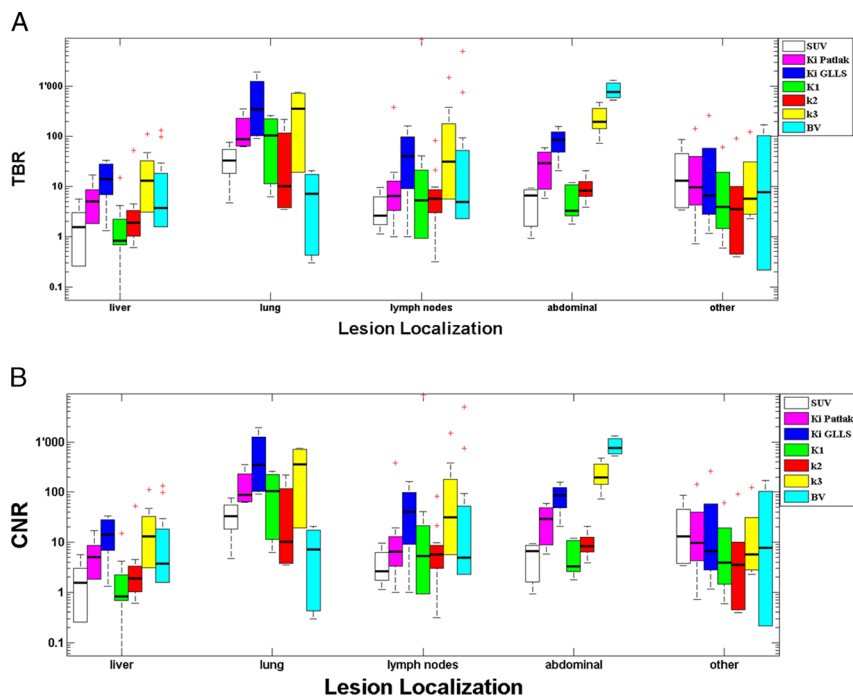
**FIGURE 6.** Whisker plots showing (**A**) TBR and (**B**) CNR for SUV, Patlak slope and intercept, $K_i$-GLLS, $K_1$, $k_2$, $k_3$, and BV-GLLS images for lesions of clinical studies located in the initial bed position.

Of the 23 malignant lesions, 18 (78%) were detected on SUV, and 18 (78%) were detected on $K_i$-Patlak. Eighteen of the 23 malignant lesions were located in the initial bed position allowing the calculation of all microparametric images ($K_i$, $K_1$, $k_2$, $k_3$). $K_i$-GLLS maps detected 14 of 18 confirmed lesions (78%), whereas $K_1$ images detected 10 of the 18 confirmed lesions (56%). $k_2$ images pinpointed 9 of 18 (50%), whereas $k_3$ images pinpointed 7 of 18 (39%). For the sake of comparison, from the 18 lesions located in the initial bed position, both SUV and $K_i$-Patlak images could detect 13 lesions (72%). The TBR and CNR scores of malignant lesions located in the initial bed position are depicted in Figure 6. The 4 lesions that were not visible on $K_i$-GLLS images included (1) a known HCC measuring $30 \times 23 \times 31$ mm$^3$ visible on the contrast-enhanced CT (patient 1), nonhypermetabolic on the SUV image (TBR = 0.34), nonhypermetabolic on $K_i$-Patlak image, nonhypermetabolic for $K_i$-GLLS image, but visible on $K_1$ image and $k_2$ image and nonvisible on $k_3$ image (Fig. 2); (2) an HCC lesion visible on contrast-enhanced CT images but not on any other modality; (3) an HCC lesion not visible on any modality except $k_2$ image (TBR = 1.79) (Fig. 3); (4) a biopsy-proven malignant HCC of the liver only detectable on $K_1$ and $k_2$ images (Fig. 4). None of these 4 lesions was detected on SUV images, similar to the HCC lesion detectable on $K_i$-GLLS, $K_1$ and $k_2$ images (Fig. 5). Meanwhile, cases where $K_i$-Patlak could not detect the lesions were matched on SUV images. Except the previous 5 determined lesions, the other 13 known and biopsy-proven malignant lesions were visible on SUV, $K_i$-Patlak, and $K_i$-GLLS but had different visibility features on $K_1$, $k_2$, and $k_3$ images.

Of the 71 probably malignant lesions, 29 lesions were located in the initial bed position part. $K_i$-GLLS detected 25 of these 29 lesions (86%), $K_1$ images could not detect any of them (0%), $k_2$ images pinpointed 2 of 29 (7%), whereas $k_3$ images detected 11 of these 29 lesions (38%). The lesions that could not be detected on $K_i$-Patlak were 3 thoracic lymph nodes, visible on SUV and $K_i$-GLLS. There were 4 thoracic lymph nodes that were only visible on $K_i$-GLLS but not on the other modalities. The only 2 probably malignant lesions that were

detectable on $k_2$ images were a gastric lymph node and a rib metastasis that could also be seen on $k_3$ images as well as SUV and $K_i$-GLLS and $K_i$-Patlak images. The only 2 biopsy-proven benign lesions were a thyroid nodule and a colon lesion. The thyroid nodule was hypermetabolic on SUV images but nonhypermetabolic on $K_i$-Patlak images (false-positive), whereas the colon lesion was visible on both SUV and $K_i$-Patlak images.

We assessed the accuracy and sensitivity for the 18 confirmed malignant lesions located in the initial bed position, considering the biopsy results as criterion standard as well as contrast-enhanced CT indication and the clinical follow-up proof of patients. In this group of lesions, the malignancy detection sensitivity increased from 13 of 18 (72%) in the case of SUV and $K_i$-Patlak images to 14 of 18 (78%) using $K_i$-GLLS imaging. As we had only 2 biopsy-confirmed benign lesions and none in the initial bed for GLLS analysis, we are unable to compare the specificity performance between SUV and $K_i$-GLLS imaging or estimate the added value of microcompartmental modeling.

## PET Metrics and Statistical Analysis of Clinical and Simulation Studies

Overall, Spearman rank correlation coefficient (ρ) was high and significant when analyzing clinical and simulated lesions on all image sets, namely, 0.761 ($P < 0.001$) for $K_{imax-Pat}$ and SUV$_{max}$, 0.808 ($P < 0.001$) for SUV$_{max}$ and $K_{imax-GLLS}$, and 0.657 ($P = 0.347$) for $K_{imax-Patlak}$ and $K_{imax-GLLS}$. Tables 3 to 6 summarize the correlations for each anatomical region, including simulated lung and liver lesions calculated for the 3 noise levels and 20 noise realizations. For clinical studies, TBR$_{Ki-Patlak}$ for 22 out of 23 malignant lesions (95.65%) were higher than TBR$_{SUV}$, whereas TBR$_{Ki-GLLS}$ were higher than the TBR$_{SUV}$ for all 23 malignant lesions (100%).

For 10 of 18 proven malignant lesions that were revealed by $K_1$ images, TBR$_{K1}$ were higher than TBR$_{SUV}$ for 4 of 10 cases (40%). For the 9 lesions detected by $k_2$ images, TBR$_{k2}$ of 6 of 9 (66.67%) were higher than TBR$_{SUV}$, whereas for the 7 malignant lesions that were detectable on $k_3$ images, all TBR$_{k3}$ scores 7/7 (100%),

**TABLE 3.** Spearman Correlation ($\rho$) and *P* Values Between SUV and Macroparametric and Microparametric Maps, Calculated for the Maximum Uptake of Lesions

| | SUV vs $K_i$-Pat | SUV vs V | SUV vs $K_i$-GLLS | SUV vs $K_1$ | SUV vs $k_2$ | SUV vs $k_3$ | SUV vs bv |
|---|---|---|---|---|---|---|---|
| Total | 0.761 ($P < 0.001$) | 0.309 ($P = 0.003$) | 0.808 ($P < 0.001$) | 0.481 ($P = 0.001$) | 0.371 ($P = 0.015$) | 0.395 ($P = 0.01$) | 0.189 ($P = 0.231$) |
| Abdominal | 0.583 ($P = 0.077$) | 0.617 ($P = 0.058$) | 0.90 ($P = 0.037$) | −0.1 ($P = 0.873$) | −0.1 ($P = 0.873$) | −0.3 ($P = 0.624$) | 0 ($P = 1$) |
| Liver | 0.972 ($P < 0.001$) | 0.406 ($P = 0.191$) | 0.846 ($P < 0.001$) | 0.804 ($P = 0.002$) | 0.573 ($P = 0.051$) | 0.664 ($P = 0.521$) | 0.014 ($P = 0.966$) |
| Lungs | 0.90 ($P = 0.037$) | 0.90 ($P = 0.037$) | 0.80 ($P = 0.2$) | 0.8 ($P = 0.2$) | 0.8 ($P = 0.2$) | 1.0 ($P < 0.001$) | 0.6 ($P = 0.4$) |
| Bones | 0.945 ($P < 0.001$) | 0.827 ($P = 0.002$) | — | — | — | — | — |
| Lymph nodes | 0.798 ($P < 0.001$) | 0.463 ($P = 0.004$) | 0.846 ($P < 0.001$) | 0.385 ($P = 0.217$) | 0.147 ($P = 0.649$) | −0.077 ($P = 0.812$) | 0.014 ($P = 0.966$) |
| Other | 0.311 ($P = 0.240$) | 0.024 ($P = 0.930$) | 0.714 ($P = 0.111$) | 0.486 ($P = 0.329$) | 0.486 ($P = 0.329$) | 0.086 ($P = 0.872$) | 0.486 ($P = 0.329$) |
| Lung (sim.) | 0.69 ($P < 0.001$) | 0.32 ($P < 0.001$) | 0.44 ($P < 0.001$) | 0.04 ($P = 0.56$) | 0.25 ($P < 0.001$) | 0.35 ($P < 0.001$) | 0.29 ($P < 0.001$) |
| Liver (sim.) | 0.22 ($P = 0.003$) | 0.32 ($P < 0.001$) | 0.25 ($P < 0.001$) | 0.20 ($P = 0.007$) | 0.22 ($P = 0.003$) | 0.18 ($P = 0.013$) | 0.07 ($P = 0.329$) |

The first rows are for clinical studies, whereas the last 2 rows are for the simulated lung and liver lesions. Correlation is deemed significant for $P < 0.001$. All values are reported for the full data set and for the lesions grouped by localization.

were higher than $TBR_{SUV}$ with large differences in magnitude (order of 2 or 3). The Friedman test showed statistically significant differences between the TBR metric for 6 modalities (SUV, $K_i$-Patlak, $K_i$-GLLS, $K_1$, $k_2$, and $k_3$) for the 18 malignant lesions located in the initial bed position ($P < 0.001$). $CNR_{Ki-Patlak}$ values were higher than $CNR_{SUV}$ values for 21 of 23 lesions (91.3%), whereas $CNR_{Ki-GLLS}$ values for all 18 proven lesions (100%) in the initial bed position were higher than $CNR_{SUV}$ values. Likewise, $CNR_{K1}$ values for 12 of 18 lesions (66.67%) were higher than $TBR_{SUV}$ values, whereas $CNR_{k2}$ values for 13 of 18 (72.22%) were higher than $CNR_{SUV}$.

Regarding the bias and SD scores for the simulated liver and lung lesions, it can be seen that for the lung lesions $k_2$ and $k_3$ have the highest bias (>9%), whereas SUV and $K_i$-Patlak had the lowest bias (<4%). For the liver lesions, the highest bias corresponds to $k_2$ images, whereas the lowest bias was achieved for $K_i$-Patlak images. Regarding the SD score, it can be seen that the highest SD is for lung lesions and $k_2$ images (between 40% and 70%), whereas the lowest NSD for simulated lung lesions is between 10% and 20% for SUV and $K_i$-Patlak images. For the liver lesions, the highest NSD was achieved by BV-GLLS (between 25% and 40%), and the lowest NSD was achieved by $K_i$-GLLS images (<10%).

## DISCUSSION

This study demonstrated that multipass hybrid WB PET imaging provides the capability of simultaneous estimation of compartmental and Patlak parametric maps from CBM data acquisition that may have the potential of improving standard-of-care SUV imaging lesion detectability in routine oncology applications.

The implemented protocol generated static SUV images, WB parametric slope and intercept Patlak images using Patlak graphical analysis, and microparametric images of $K_i$, $K_1$, $k_2$, $k_3$, and bv for the initial bed position in a single session, thus allowing direct comparisons between the modalities. Microparametric images can be produced for only 1 bed position, yet, lesions located anywhere in the thoracoabdominal region can be targeted because of the ability of extracting the IF from the heart or the aorta. The produced images were all of acceptable quality and all malignant lesions visible in SUV images were also detectable on $K_i$-Patlak and $K_i$-GLLS images. Furthermore, microparametric images proved to be superior in 4 HCC lesions, 3 detected on $K_1$ and $k_2$ images (Figs. 2, 4, and 5), and only 1 detected on $k_2$ images (Fig. 3). In addition, 1 biopsy-proven benign thyroid lesion, positive on SUV image, was not detectable on $K_i$-Patlak images.

In parametric Patlak and GLLS images, the $^{18}$F-FDG signal in organs including blood compartment is suppressed, and this feature results in higher contrast and thus higher TBR in these regions and neighboring organs, especially for $K_i$-Patlak, $k_i$-GLLS, and $k_3$ images. Consistent with previous studies,[2,3,21–25] the higher TBR values of $K_i$-GLLS and $k_3$ images in the liver were obvious in both clinical and simulation studies.

Although graphical Patlak analysis is a fast approach with low complexity that can be easily adopted in the clinic, it does not produce all model parameters. Detailed knowledge of all parameters reflecting tracer kinetics is ideally required for a complete understanding of the physiological process being studied.[26] Through the survey of malignant lesions, it became clear that despite the limited axial coverage for the targeted axial FOV

**TABLE 4.** Spearman Correlation ($\rho$) and *P* Values Between Ki-Patlak and Microparametric Images, Calculated for the Maximum Values of Lesions

| | $K_i$-Pat vs $K_i$-GLLS | $K_i$-Pat vs $K_1$ | $K_i$-Pat vs $k_2$ | $K_i$-Pat vs $k_3$ | $K_i$-Pat vs bv |
|---|---|---|---|---|---|
| Total | 0.791 ($P < 0.001$) | 0.388 ($P = 0.011$) | 0.319 (0.039) | 0.356 ($P = 0.021$) | 0.109 ($P = 0.493$) |
| Abdominal | 0.4 ($P = 0.505$) | −0.6 ($P = 0.285$) | −0.1 ($P = 0.873$) | −0.7 ($P = 0.188$) | −0.3 ($P = 0.624$) |
| Liver | 0.916 ($P < 0.001$) | 0.783 ($P = 0.003$) | 0.538 ($P = 0.071$) | 0.713 ($P = 0.009$) | 0.067 ($P = 0.837$) |
| Lungs | 1.0 ($P < 0.001$) | 1.0 ($P < 0.001$) | 0.6 ($P = 0.4$) | 0.8 ($P = 0.2$) | 0.8 ($P = 0.2$) |
| Lymph nodes | 0.748 ($P = 0.005$) | 0.497 ($P = 0.101$) | 0.245 ($P = 0.443$) | −0.091 ($P = 0.779$) | 0.014 ($P = 0.966$) |
| Other | 0.657 ($P = 0.156$) | −0.086 ($P = 0.872$) | −0.086 ($P = 0.872$) | 0.714 ($P = 0.111$) | 0.2 ($P = 0.704$) |
| Lung (sim.) | 0.56 ($P < 0.001$) | −0.02 ($P = 0.750$) | 0.07 ($P = 0.374$) | 0.42 ($P < 0.001$) | 0.20 ($P = 0.006$) |
| Liver (sim.) | 0.61 ($P < 0.001$) | 0.16 ($P = 0.027$) | 0.14 ($P = 0.055$) | 0.22 ($P = 0.003$) | 0.24 ($P = 0.001$) |

The first rows are for clinical studies, whereas the last 2 rows are for the simulated lung and liver lesions. Correlation is deemed significant for $P < 0.01$. All values are reported for the full data set and for the lesions grouped by localization.

**TABLE 5.** Spearman Correlation (ρ) and *P* Values Between SUV and Macroparametric and Microparametric Images, Calculated for the Mean Values of Background

| | SUV and $k_i$-Pat | SUV and bv-Pat | SUV and $K_i$-GLLS | SUV and $K_1$ | SUV and $k_2$ | SUV and $k_3$ | SUV and bv-GLLS |
|---|---|---|---|---|---|---|---|
| Total | 0.572 ($P < 0.001$) | 0.781 ($P < 0.001$) | 0.217 ($P = 0.167$) | 0.471 ($P = 0.002$) | 0.045 ($P = 0.777$) | −0.652 ($P < 0.001$) | −0.531 ($P < 0.001$) |
| Abdominal | 0.465 ($P = 0.352$) | 0.96 ($P = 0.002$) | — | −0.5 ($P = 0.667$) | — | — | 0.5 ($P = 0.667$) |
| Liver | 0.809 ($P = 0.001$) | 0.782 ($P = 0.003$) | 0.256 ($P = 0.422$) | −0.674 ($P = 0.016$) | −0.791 ($P = 0.002$) | 0.256 ($P = 0.422$) | 0.244 ($P = 0.445$) |
| Lungs | 0.90 ($P = 0.061$) | 0.30 ($P = 0.624$) | 0.40 ($P = 0.6$) | −0.40 ($P = 0.6$) | 0.40 ($P = 0.6$) | 0.40 ($P = 0.6$) | 0.80 ($P = 0.2$) |
| Bones | 0.68 ($P = 0.021$) | 0.763 ($P = 0.006$) | — | — | — | — | — |
| Lymph nodes | 0.535 ($P < 0.001$) | 0.70 ($P < 0.001$) | 0.31 ($P = 0.327$) | 0.39 ($P = 0.21$) | −0.011 ($P = 0.974$) | −0.224 ($P = 0.484$) | −0.459 ($P = 0.133$) |
| Other | 0.251 ($P = 0.348$) | 0.456 ($P = 0.076$) | 0.714 ($P = 0.111$) | 0.486 ($P = 0.329$) | 0.486 ($P = 0.329$) | −0.086 ($P = 0.872$) | −0.486 ($P = 0.329$) |
| Lung (sim.) | −0.07 ($P = 0.600$) | 0.13 ($P = 0.320$) | 0.04 ($P = 0.760$) | 0.12 ($P = 0.378$) | 0.01 ($P = 0.924$) | −0.11 ($P = 0.385$) | −0.13 ($P = 0.318$) |
| Liver (sim.) | 0.02 ($P = 0.889$) | −0.05 ($P = 0.659$) | 0.05 ($P = 0.678$) | −0.09 ($P = 0.482$) | −0.03 ($P = 0.795$) | 0.07 ($P = 0.616$) | 0.15 ($P = 0.266$) |

The first rows are for clinical studies, whereas the last 2 rows are for the simulated lung and liver lesions. Correlation is deemed significant for $P < 0.01$. The values are reported for the full data set and for the lesions grouped by localization.

supposed to contain the pathology for which microparametric maps were generated, these images provide additional relevant information. The 4 HCC lesions not visible on SUV images but detected on microparametric maps strongly support the complementary role of microcompartmental modeling. Another finding of this study regarding the model parameters is that although lesion detectability of $k_3$ images is relatively low (39%), these images produce superior TBR, suggesting their potential for lesion delineation and segmentation. Strauss et al[27] also mentioned that $k_3$ maps might be useful and have been used for supporting the volume-of-interest positioning. Finally, the biopsy-proven benign thyroid lesion, positive on SUV images but negative on $K_i$ and microparametric images, is in line with previous observations supporting the fact that $K_i$ imaging has the potential to reduce false-positives.[21]

We found strong positive correlations between $K_{imax-Patlak}$ and $SUV_{max}$ (ρ = 0.761), between $K_{imax-GLLS}$ and $SUV_{max}$ (ρ = 0.808), and between $K_i$-Patlak and $K_i$-GLLS (ρ = 0.791) and even stronger correlations when looking separately at different organs, such as the liver, bones, and lymph nodes. The simulation results also indicate good correlations between SUV and $K_i$-Patlak, SUV and $K_i$-GLLS, and $K_i$-Patlak and $K_i$-GLLS for lung and liver lesions (Tables 3 and 4). This is an indication that $K_i$-Patlak and $K_i$-GLLS images will identify hypermetabolic lesions if they are depicted on SUV images. However, there were weak correlations between SUV and $K_i$-Patlak and also SUV and $K_i$-GLLS in background neighboring regions in both clinical and simulation studies. This was expected because of blood pool suppression in $K_i$ images.

Tumor-to-background ratio and CNR scores for malignant lesions were higher for $K_i$-GLLS and $K_i$-Patlak images than SUV images (Fig. 7). $k_3$ Images also show higher TBR than SUV images owing to suppressed background. Considering malignant and probably malignant lesions, the TBR of $K_i$-Patlak is higher than SUV images (Fig. 8), although 5 individual cases had higher TBRs on SUV images compared with $K_i$-Patlak images. Four of them were Hodgkin lymphoma lesions (bone and nodal), whereas the last one was a retroperitoneal nodal metastasis of a cholangiocarcinoma. The CNR of malignant and probably malignant lesions was higher for $K_i$-Patlak than SUV images (Fig. 8). Figure 6 shows that more or less TBR and CNR scores for $K_i$ GLLS are higher comparing to other modalities ($P < 0.001$). Tumor-to-background ratio and CNR scores of $K_1$ and $k_2$ images are commonly higher than SUV images, which partly explains their better lesion detectability. Although in simulation studies the TBR and CNR scores of $K_1$ and $k_2$ images for liver lesions are lower than SUV, $K_i$-Patlak, $K_i$-GLLS, and $k_3$ images, drawing any conclusions is difficult given that only 1 type of liver lesions was modeled contrary to clinical situations where there are a variety of liver lesions with different indications, grades, and physiologies.

The bias and NSD metrics calculated for simulated lung and liver lesions demonstrated that the bias for $k_2$ images is the highest among other parameters and that SUV and $K_i$-Patlak images have the lowest bias for lung and liver lesions. For lung lesions, the highest SD was associated with $k_2$ images, whereas the lowest NSD was associated with SUV and $K_i$-Patlak images. Likewise,

**TABLE 6.** Spearman Correlation (ρ) and *P* Values (Sig. 2-Tailed) Between Ki-Patlak and Microparametric Images, Calculated for the Mean Values of Background

| | $K_i$-Pat and $K_i$-GLLS | $K_i$-Pat and $K_1$ | $K_i$-Pat and $k_2$ | $K_i$-Pat and $k_3$ | $K_i$-Pat and bv_GLLS |
|---|---|---|---|---|---|
| Total | 0.65 ($P < 0.001$) | 0.519 ($P < 0.001$) | 0.068 ($P = 0.668$) | −0.378 ($P = 0.013$) | −0.348 ($P = 0.024$) |
| Abdominal | −0.50 ($P = 0.667$) | — | 0.50 ($P = 0.667$) | −0.50 ($P = 0.667$) | 0.50 ($P = 0.667$) |
| Liver | 0.162 ($P = 0.615$) | −0.532 ($P = 0.075$) | −0.74 ($P = 0.006$) | 0.162 ($P = 0.615$) | 0.433 ($P = 0.16$) |
| Lungs | 0.40 ($P = 0.60$) | −0.40 ($P = 0.60$) | 0.40 ($P = 0.60$) | 0.40 ($P = 0.60$) | 0.80 ($P = 0.20$) |
| Lymph nodes | 0.743 ($P = 0.006$) | 0.66 ($P = 0.019$) | 0.34 ($P = 0.28$) | −0.807 ($P = 0.002$) | −0.871 ($P < 0.001$) |
| Other | 0.657 ($P = 0.156$) | 0.086 ($P = 0.872$) | 0.086 ($P = 0.872$) | 0.714 ($P = 0.111$) | 0.20 ($P = 0.704$) |
| Lung (sim.) | 0.58 ($P < 0.001$) | 0.26 ($P = 0.042$) | 0.44 ($P < 0.001$) | 0.66 ($P < 0.001$) | 0.03 ($P = 0.816$) |
| Liver (sim.) | 0.51 ($P < 0.001$) | 0.12 ($P = 0.368$) | 0.15 ($P = 0.244$) | 0.39 ($P = 0.002$) | −0.16 ($P = 0.002$) |

The first rows are for clinical studies, whereas the last 2 rows are for the simulated lung and liver lesions. Correlation is deemed significant for $P < 0.01$. All values are reported for the full data set and for the lesions grouped by localization.
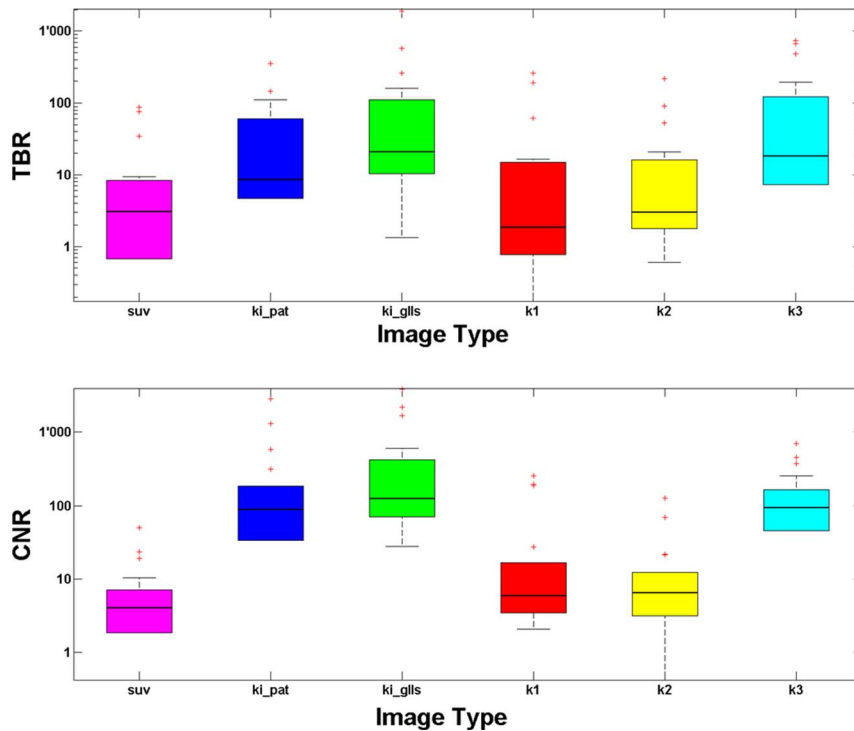
**FIGURE 7.** TBR and CNR whisker plots showing TBR for the 18 malignant lesions of clinical studies located in the initial bed position.

for liver lesions, it was observed that BV-GLLS had the highest NSD scores among the different modalities, whereas $K_i$-GLLS had the lowest NSD.

    SUV and $K_i$ images can be equivalent under 2 special circumstances.[8] The first condition is when the blood volume is negligible or when specific uptake far outbalances the background uptake.

The second condition is the proportionality of the integral of plasma IF (PIF) ($\int_0^t C_p(\tau)d\tau$) to the SUV (injected activity divided by the patient's weight). The first condition will be invalid for less FDG-avid tumors or for lesions located in organs with a larger fraction of blood volume, or when high physiologic (nonspecific) uptake may interfere with disease-specific uptake in the same tissue. For
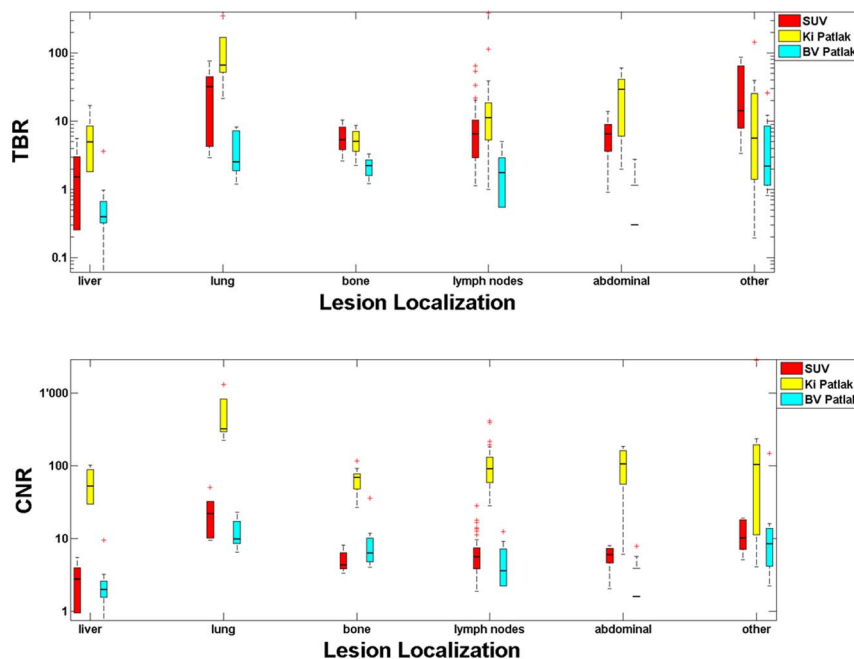


**FIGURE 8.** Whisker plots showing TBR and CNR for the SUV and Patlak slope and intercepts images for all malignant and probably malignant lesions of the clinical studies.

less FDG-avid tumors or lesions located in organs, such as the liver, these 2 parameters cannot be equivalent, and the higher performance of $K_i$ images than SUV images in terms of lesion detectability is mainly due to the blood-volume suppression. The second condition verifies when tracer infiltration or extravasation occurs at the injection site, affecting the relationship between the PIF integral (radiotracer quantity available for uptake) and the total administered dosage, or when the PIF is modified after a treatment regimen (such as chemotherapy or hormone therapy) or by an altered cardiac output. In these cases, SUV images cannot take PIF modification into account, whereas $K_i$ imaging is able to account for these changes.

Hence, from a theoretical standpoint, we can expect that when the 2 conditions are fulfilled, SUV and $K_i$ images will have comparable performances, and when these conditions cannot be fulfilled, $K_i$ images will have an advantage over SUV images. Our results are in agreement with these postulates. However, we should keep in mind that some lesions remain undetectable on SUV, macrocompartmental, and microcompartmental images. One such example is the case of an HCC liver lesion that was detectable only on contrast-enhanced CT images. Another aspect that deserves particular attention is that parametric imaging improves quantification, an important asset that static semiquantitative SUV imaging can hardly cope with. Moreover, our findings show that the higher TBR and CNR scores do not necessarily result in improved lesion detectability. In the previously described 4 HCC lesions, the high TBR and CNR scores do not always reflect that a lesion is detected, because of the different noise and background levels involved. The 2 main reasons are as follows: (i) the noise characteristics of the images, because 1 noisy pixel in the ROI is sufficient to obtain a high TBR score even if the lesion is not visible; (ii) in case of extremely low background, even a low noise pixel in an ROI can produce a large TBR or CNR score. Therefore, the visual appreciation for lesion detectability is mandatory.

The main limitation of this study is the small number of patients and of biopsy-proven lesions, a common issue encountered in clinical research. From a methodological standpoint, neglecting $k_4$ parameter in our analysis may have resulted in quantification errors in few organs, such as the liver.[28] Yet, it has been reported that the irreversible model is sufficient for describing the tissue time-activity curves when the scan duration is less than 60 minutes,[29–31] as in our case.

## CONCLUSIONS

This work investigated lesion detectability features when using various microcompartmental and macrocompartmental maps and compared them with standard-of-care SUV images. Multipass WB PET parametric imaging utilizing graphical Patlak and GLLS analysis outperformed conventional SUV imaging, specifically for the detectability of HCC lesions. The image-derived metrics for the different modalities were significantly correlated, yet the suppression of nonspecific ^{18}F-FDG signal in the blood compartment resulted in higher TBR and CNR scores in parametric images as compared with SUV images. This work will be continued by enrolling additional patients to increase the sample size, including different primary tumors to verify if our observations are associated with specific histological types.

## REFERENCES

1. Kotasidis F, Tsoumpas C, Rahmim A. Advanced kinetic modelling strategies: towards adoption in clinical PET imaging. *Clin Transl Imaging*. 2014;2:219–237.

2. Karakatsanis NA, Lodge MA, Tahari AK, et al. Dynamic whole-body PET parametric imaging: I. Concept, acquisition protocol optimization and clinical application. *Phys Med Biol*. 2013;58:7391–7418.

3. Karakatsanis NA, Casey ME, Lodge MA, et al. Whole-body direct 4D parametric PET imaging employing nested generalized Patlak expectation-maximization reconstruction. *Phys Med Biol*. 2016;61:5456–5485.

4. Zhu W, Li Q, Bai B, et al. Patlak image estimation from dual time-point list-mode PET data. *IEEE Trans Med Imaging*. 2014;33:913–924.

5. Avril N, Bense S, Ziegler SI, et al. Breast imaging with fluorine-18-FDG PET: quantitative image analysis. *J Nucl Med*. 1997;38:1186–1191.

6. Dimitrakopoulou-Strauss A, Strauss LG, Heichel T, et al. The role of quantitative (18)F-FDG PET studies for the differentiation of malignant and benign bone lesions. *J Nucl Med*. 2002;43:510–518.

7. Shreve PD, Anzai Y, Wahl RL. Pitfalls in oncologic diagnosis with FDG PET imaging: physiologic and benign variants. *Radiographics*. 1999;19:61–77; quiz 150–151.

8. Rahmim A, Lodge MA, Karakatsanis NA, et al. Dynamic whole-body PET imaging: principles, potentials and applications. *Eur J Nucl Med Mol Imaging*. 2019;46:501–518.

9. Adams MC, Turkington TG, Wilson JM, et al. A systematic review of the factors affecting accuracy of SUV measurements. *AJR Am J Roentgenol*. 2010;195:310–320.

10. Freedman NM, Sundaram SK, Kurdziel K, et al. Comparison of SUV and Patlak slope for monitoring of cancer therapy using serial PET scans. *Eur J Nucl Med Mol Imaging*. 2003;30:46–53.

11. Hamberg LM, Hunter GJ, Alpert NM, et al. The dose uptake ratio as an index of glucose metabolism: useful parameter or oversimplification? *J Nucl Med*. 1994;35:1308–1312.

12. Huang SC. Anatomy of SUV. Standardized uptake value. *Nucl Med Biol*. 2000;27:643–646.

13. Strauss LG. Fluorine-18 deoxyglucose and false-positive results: a major problem in the diagnostics of oncological patients. *Eur J Nucl Med*. 1996;23:1409–1415.

14. Zaidi H, Karakatsanis N. Towards enhanced PET quantification in clinical oncology. *Br J Radiol*. 2018;91:20170508.

15. Czernin J, Allen-Auerbach M, Schelbert HR. Improvements in cancer staging with PET/CT: literature-based evidence as of September 2006. *J Nucl Med*. 2007;48:78S–88S.

16. Kotasidis FA, Matthews JC, Reader AJ, et al. Application of adaptive kinetic modelling for bias propagation reduction in direct 4D image reconstruction. *Phys Med Biol*. 2014;59:6061–6084.

17. Kotasidis FA, Garibotto V, Zaidi H. Hybrid whole-body dynamic TOF PET imaging for simultaneous estimation of compartmental and Patlak parametric maps from continuous bed motion data. In: *Presented at the IEEE Nuclear Science Symposium and Medical Imaging Conference (NSS/MIC)*. Strasbourg, France; October 29–November 6, 2016.

18. Karakatsanis N, Rahmim A, Lodge M, et al. Introducing time-of-flight and resolution recovery image reconstruction to whole-body PET parametric imaging. In: *Presented at the Nuclear Science Symposium and Medical Imaging Conference (NSS/MIC)*. Seattle, WA; November 8–15, 2014.

19. Segars W, Sturgeon G, Mendonca S, et al. 4D XCAT phantom for multimodality imaging research. *Med Phys*. 2010;37:4902–4915.

20. Kotasidis FA, Tsoumpas C, Polycarpou I, et al. A 5D computational phantom for pharmacokinetic simulation studies in dynamic emission tomography. *Comput Med Imaging Graph*. 2014;38:764–773.

21. Fahmi G, Karakatsanis N, Di Domenicantonio G, et al. Does whole-body Patlak ^{18}F-FDG PET imaging improve lesion detectability in clinical oncology? *Eur Radiol*. 2019;29:4812–4821.

22. Karakatsanis NA, Lodge MA, Zhou Y, et al. Dynamic whole-body PET parametric imaging: II. Task-oriented statistical estimation. *Phys Med Biol*. 2013;58:7419–7445.

23. Karakatsanis NA, Zhou Y, Lodge MA, et al. Generalized whole-body Patlak parametric imaging for enhanced quantification in clinical PET. *Phys Med Biol*. 2015;60:8643–8673.

24. Ilan E, Sandstrom M, Velikyan I, et al. Parametric net influx rate images of (68)Ga-DOTATOC and (68)Ga-DOTATATE: quantitative accuracy and improved image contrast. *J Nucl Med*. 2017;58:744–749.

25. Zhuang M, Karakatsanis NA, Dierckx R, et al. Quantitative analysis of heterogeneous ^{18}F-FDG static (SUV) vs. Patlak ($K_i$) whole-body PET imaging using different segmentation methods: a simulation study. *Mol Imaging Biol*. 2019;21:317–327.

26. Chen K, Lawson M, Reiman E, et al. Generalized linear least squares method for fast generation of myocardial blood flow parametric images with N-13 ammonia PET. *IEEE Trans Med Imaging*. 1998;17:236–243.

27. Strauss LG, Klippel S, Pan L, et al. Assessment of quantitative FDG PET data in primary colorectal tumours: which parameters are important with respect to tumour detection? *Eur J Nucl Med Mol Imaging*. 2007;34:868–877.

28. Dimitrakopoulou-Strauss A, Georgoulias V, Eisenhut M, et al. Quantitative assessment of SSTR2 expression in patients with non–small cell lung cancer using(68)Ga-DOTATOC PET and comparison with (18)F-FDG PET. *Eur J Nucl Med Mol Imaging*. 2006;33:823–830.

29. Dhawan V, Moeller JR, Strother SC, et al. Effect of selecting a fixed dephosphorylation rate on the estimation of rate constants and rCMRGlu from dynamic [$^{18}$F] fluorodeoxyglucose/PET data. *J Nucl Med*. 1989; 30:1483–1488.

30. Ikoma Y, Watabe H, Shidahara M, et al. PET kinetic analysis: error consideration of quantitative analysis in dynamic studies. *Ann Nucl Med*. 2008;22:1–11.

31. Taguchi A, Toyama H, Kimura Y, et al. Comparison of the number of parameters using nonlinear iteration methods for compartment model analysis with $^{18}$F-FDG brain PET. *Kaku Igaku*. 1997;34:25–34.